

Date of publication xxxx 00, 0000, date of current version xxxx 00, 0000.

Digital Object Identifier 10.1109/ACCESS.2024.0429000

# ARUC-GAN: A CycleGAN-Based Attention Residual U-Net for Low-Dose CT Denoising in Smart Healthcare

MOHAMMAD MANSOUR<sup>1</sup>, DJAMEL DJENOURI<sup>2</sup>, LOBNA A. SAID<sup>3</sup>, SHAHID LATIF<sup>2</sup>, AHMED MAALEL<sup>4</sup>, AMEER M. S. ABDELHADI<sup>1</sup>

<sup>1</sup>Department of Electrical and Computer Engineering, McMaster University, Hamilton, L8S 4L8, ON, Canada. Emails: mansom54@mcmaster.ca, ameerm@mcmaster.ca

<sup>2</sup>University of the West of England, Bristol, UK. Emails: Djamel.Djenouri@uwe.ac.uk, Shahid.Latif@uwe.ac.uk

<sup>3</sup>Nanoelectronics Integrated Systems Center (NISC), Nile University, Giza 12588, Egypt. Email: l.a.said@ieee.org

<sup>4</sup>University of Sousse, ISSAT Sousse, RIADI Laboratory, National School of Computer Science, ENSI, Tunisia. Email: ahmed.maalel@ensi.mu.tn

Corresponding author: Djamel Djenouri (e-mail: Djamel.Djenouri@uwe.ac.uk).

This work was supported by the Arab-German Young Academy of Sciences and Humanities (AGYA). AGYA draws on support from the German Federal Ministry of Education and Research (BMBF; grant no. 01DL20003).

**ABSTRACT** Low-dose computed tomography (LDCT) is increasingly adopted in medical imaging to minimize radiation exposure. However, the diagnostic accuracy is primarily affected by different noise sources, e.g., quantum, electronic, and reconstruction. Moreover, conventional denoising methods struggle with the non-uniform noise distributions in LDCT images and often require complex projection data, which limits their effectiveness and generalizability. Herein, we propose an AI-based denoising approach using an Attention Residual U-Net (ARU-Net) architecture integrated into the CycleGAN framework named Attention Residual U-Net CycleGAN (ARUC-GAN). The proposed framework outperforms state-of-the-art denoising models, such as RED-CNN, EDCNN, and CTformer, according to experimental evaluation on the Mayo Clinic abdominal CT dataset. The model exhibits a peak signal-to-noise ratio (PSNR) of 34.82 dB, a structural similarity index (SSIM) of 0.85, and an RMSE of 0.018. Furthermore, the model successfully maintains edge structures with an Edge Keeping Index (EKI) of 0.835. The visual examination validates ARUC-GAN's superior texture and detail preservation. The results indicate that the suggested method has great promise as a smart health tool for improving diagnosis accuracy in LDCT scans.

**INDEX TERMS** Smart Healthcare, Artificial Intelligence, GAN, Image Processing, Medical Imaging.

## I. INTRODUCTION

The healthcare sector is undergoing a digital transformation propelled by advancements in artificial intelligence (AI) and the Internet of Medical Things (IoMT) [1]–[3]. These technologies have paved the way for smart health applications that enhance patient care through advanced diagnostics, wearable devices, and intelligent systems [4], [5]. A key area of impact is medical imaging, where these technologies are now enhancing foundational modalities such as computed tomography (CT) [6]. As a cornerstone of modern diagnostics, CT imaging provides high-resolution, cross-sectional views of internal anatomy. However, the widespread use of CT imaging introduces risks associated with X-ray radiation exposure. Common clinical CT procedures deliver significant radiation doses from lung screenings (1.5 mSv) to coronary angiography with contrast enhancement (24 mSv). These exposures

exceed natural annual background levels ( $\sim 3$  mSv) [7], as shown in Fig. 1. Prolonged or repeated exposure has been linked to cumulative DNA damage and potential carcinogenic effects [8]. This has underscored the need for safer imaging protocols such as low-dose CT (LDCT).

Besides expediting scanning procedures, LDCT reduces the ionizing radiation exposure by fine-tuning tube voltage, tube current, and pitch settings. However, LDCT images often suffer from significant degradation in quality due to noise originating from quantum, electronic, and reconstruction processes [9]. Quantum noise, caused by statistical fluctuations in X-ray photon detection, produces a grainy image texture, while electronic and reconstruction noise introduces additional artifacts [10]. These issues can obscure critical anatomical details, directly impacting diagnostic accuracy. For example, quantum noise can blur small lung nodules, affect-

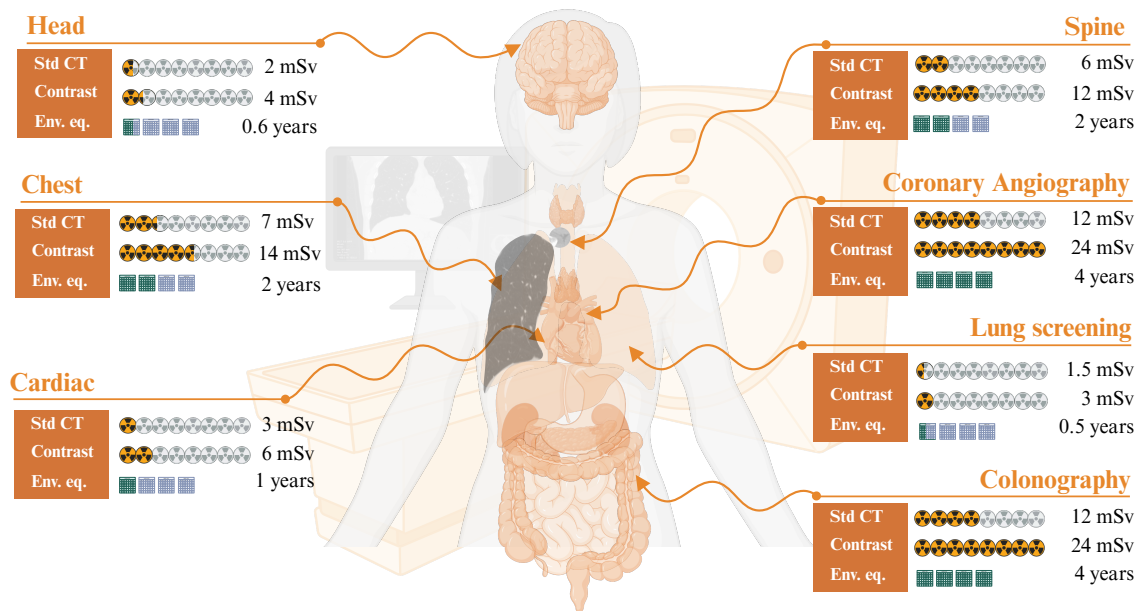


**FIGURE 1. Radiation absorption levels (mSv) for standard and contrast-enhanced CT scans, with equivalent environmental radiation exposure times, across different human body regions.**

ing early cancer detection [11], while electronic noise may mask fine bone fractures, complicating diagnosis [12]. Non-uniform noise can also hinder the identification of ischemic areas in brain scans, crucial for stroke diagnosis, and reduce contrast in abdominal imaging, making tumor detection difficult [13]. Additionally, reconstruction artifacts in vascular imaging may conceal small or occluded vessels, limiting the effectiveness of angiographic assessments [14]. Thus, image denoising is applied as an essential preprocessing step to enhance the quality of denoised LDCT images. Denoising makes the next image processing tasks, like segmentation and feature extraction, more accurate by getting rid of noise while keeping fine anatomical structures. This contributes to more reliable clinical interpretations and improved diagnostic outcomes in smart healthcare applications.

Conventional denoising methods, such as sinogram domain filtering and iterative reconstruction techniques, have been developed to address these challenges. However, these approaches rely heavily on access to original projection data and are computationally intensive. Furthermore, they cannot generalize effectively across diverse noise patterns due to the non-uniform noise distribution in LDCT images [15]. Given the limitations of conventional denoising techniques, AI-based methods have emerged as a promising alternative for enhancing LDCT image quality. These methods leverage high performance to process LDCT images and effectively reduce noise without requiring the original projection data. As illustrated in Fig. 2, AI-based denoising operates on the image domain, transforming cross-sectional LDCT images into high-quality, denoised scans. This approach addresses the challenges associated with acquiring projection data. It adapts to the complex, non-uniform noise distributions characteris-

tic of LDCT images, offering improved generalizability and performance over traditional techniques.

This article introduces a novel denoising framework, the Attention Residual U-Net CycleGAN (ARUC-GAN), which introduces a dual-generator and dual-discriminator architecture to enhance LDCT image quality. The dual generators facilitate bidirectional image translation between noisy LDCT and clean full-dose CT (FDCT) domains, ensuring that cycle consistency is maintained for structural accuracy. Simultaneously, the dual discriminators rigorously assess the realism of generated images, providing adversarial feedback that sharpens fine details and improves image fidelity. By integrating attention and residual mechanisms within the CycleGAN framework, ARUC-GAN outperforms existing models. Experimental results reveal that the proposed model achieves superior performance across key metrics such as peak signal-to-noise ratio (PSNR), structural similarity index (SSIM), and root mean square error (RMSE). Furthermore, visual evaluations highlight its capability to preserve crucial textures and intricate details.

The rest of the paper is organized as follows: Section II reviews state-of-the-art LDCT denoising methods, and both supervised and unsupervised machine learning techniques are covered. Section III details the methodology, dataset, and the ARUNet-Cycle-GAN architecture. Section IV presents and analyzes the proposed architectures using various metrics for evaluation. Section V discusses conclusions and future directions.

## II. RELATED WORK

Iterative reconstruction has significantly reduced radiation dose in CT imaging while mitigating noise to some extent.

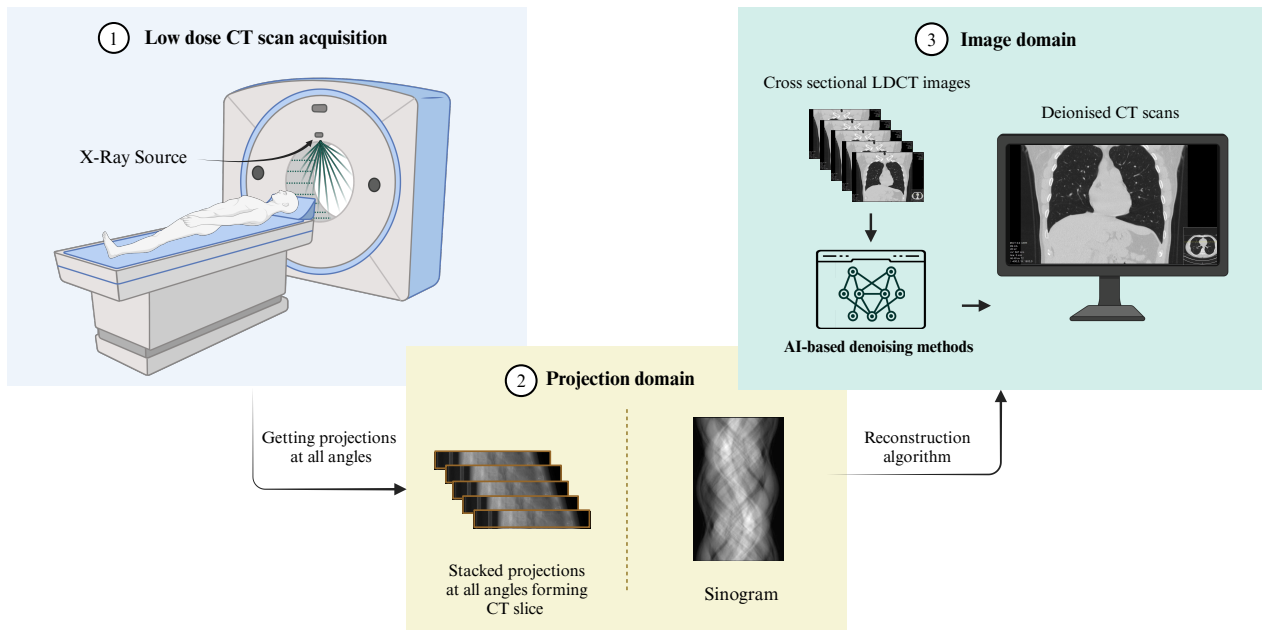


**FIGURE 2. Schematic representation of low-dose CT scan acquisition and reconstruction process. The diagram illustrates the steps from X-ray source emission, projection domain processing, and the formation of CT slice sinograms to the generation of cross-sectional LDCT images. AI-based denoising methods are applied to deionized CT scans to enhance image quality.**

However, AI-driven denoising, particularly deep learning (DL), offers a transformative solution [16]. Convolutional neural networks (CNNs) excel at learning complex patterns directly from data, making them well-suited for LDCT denoising. These networks, trained in a supervised manner with LDCT inputs and NDCT targets, have been enhanced through various techniques. Some studies utilize standard CNNs [17], while others apply preprocessing methods like wavelet-domain transformations [18] or Sobel filters for edge detection [19]. Post-processing strategies, such as cost function refinement via Sobel detection [20], further improve results. Residual connections help mitigate gradient-related issues [21], and alternative architectures, including DenseNet with residual [22] or skip connections [19], have demonstrated efficacy.

Advanced methodologies include cascaded CNNs, where multi-stage networks progressively refine outputs [23]–[25], and multi-parallel processing, which merges outputs from parallel networks for enhanced denoising [26]. Dilated convolutions improve the perceptual field without increasing parameters [27], often integrated with residual learning [28]. Hybrid approaches combine these techniques, such as parallel dilated networks for multi-scale feature extraction [29] or residual-dilated architectures with multiple dilation rates [30]. To exploit spatial relationships, 3D ResNet-based models process adjacent CT slices [31], [32]. Beyond CNNs, Panigrahi et al. [33] introduced CTuNLM, leveraging curvelet transforms, NLM filtering, and scale-dependent thresholding to preserve fine details. Their "Deep Curvelet-Net" integrates multiscale spatial features with attention

mechanisms for enhanced denoising. Additionally, they proposed phase-preserved curvelet thresholding (PPCT) [34], which employs adaptive Wiener filtering in coarser scales and bilateral filtering at finer scales for better edge localization and artifact suppression. Mathematical analysis confirms its superior noise immunity over magnitude-based thresholding. Other studies include state-space models (SSMs) with encoder-decoder structures such as DenoMamba and I2I-Mamba. This enhances the capture of both short- and long-range spatial and channel dependencies [35], [36].

Most CNN and encoder-decoder models use Mean Square Error (MSE) as a loss function, which often leads to blurred images due to ignored texture details. Generative Adversarial Networks (GANs) address this by incorporating adversarial loss, minimizing JS or KL divergence to enhance edge preservation and fine details [37]. However, GANs struggle with effective noise suppression, prompting researchers to explore multi-loss approaches. For instance, [38] combined MSE with generator loss for sharper images, while [39] integrated adversarial, L1, and structural losses to counter over-smoothing. Similarly, [40] improved GAN performance by incorporating least squares, structural similarity, and L1 loss. Training instability, including mode collapse, is a common GAN challenge. Wasserstein GAN (WGAN), using Wasserstein distance as a loss function, was first applied to LDCT denoising by [41] with perceptual loss. WGAN has since been widely adopted; [42] introduced a model with four loss functions—Wasserstein distance, perceptual loss, sharpness loss, and structural similarity loss. Additionally, replacing cross-entropy loss with least square loss mitigates gradient

penalties, while pre-trained models like VGG and ResNet enhance GAN performance with perceptual loss.

Hybrid architectures further refine GAN-based denoising. In [43], a dual U-Net generator separates general image generation from high-frequency component mapping. Similarly, [44] proposed a dual-generator framework for noise and texture distribution learning. A novel U-Net-based generator with multiple discriminators along deconvolution layers was introduced in [45], forming a joint discriminator. Conversely, [46] employed a dual-network U-Net discriminator, where one network captures input-target differences and the other focuses on gradient map variations between LDCT and NDCT. Another layer of improvement is introduced by employing Cycle-GAN, which does not require paired training datasets while also enforcing the learned mapping with higher accuracy through its cycle consistency loss. [47] utilized Cycle-GAN with cycle-consistency loss alongside identity loss to generate images without artifacts more effectively. Furthermore, [48] proposed a similar Cycle-GAN approach, incorporating prior image information and merging the losses of both models with the traditional denoising algorithm BM3D, thereby enhancing denoising performance.

To overcome the shortcomings of existing studies, the proposed ARUC-GAN integrates attention and residual mechanisms into a CycleGAN framework. This hybrid approach leverages the strengths of attention for feature prioritization, residual connections for efficient training, and CycleGAN for unpaired domain translation. Unlike conventional and earlier AI-based methods, ARUC-GAN achieves superior denoising performance without relying on projection data, offering a scalable and generalizable solution for smart health applications.

### III. METHODOLOGY

The proposed approach for denoising LDCT images combines the strengths of attention mechanisms, residual learning, and GANs to enhance image quality while preserving fine details. The methodology's core is the development of the ARU-Net architecture to serve as the generator within a CycleGAN framework. The ARU-Net leverages the encoder-decoder structure of U-Net, attention, and residual mechanisms to capture and retain critical features effectively. Integrating ARU-Net into the CycleGAN framework enables robust noise reduction and image reconstruction. The target of the proposed framework is post-reconstruction restoration for LDCT scans. To achieve this, the model is trained on the Mayo Clinic DICOM dataset. This section details the architecture, training process, and evaluation metrics used to validate the performance of the proposed models.

#### A. DATASET SPECIFICATION

The dataset employed is derived from LDCT Grand Challenge and the publicly available library hosted by The Cancer Imaging Archive (TCIA) [49]. It encompasses data from 299 anonymized patient CT exams, including scans of the head, chest, and abdomen. These cases are evenly split be-

tween Siemens SOMATOM Definition Flash and GE Light-speed VCT CT scanners, each contributing approximately 50% of the dataset. The dataset includes three key types of data: DICOM-CT-PD projection data, reconstructed CT image data, and associated clinical reports. The DICOM-CT-PD format, an open and vendor-neutral standard, encodes critical projection and acquisition geometry data. For evaluation, test datasets included a range of patient sizes and conditions. Participants were provided either projection data or 1-3 mm thick reconstructed images with a choice between medium (B30) and sharp (D45) reconstruction kernels. The Hounsfield Unit (HU) range of the dataset, spanning from -1024 HU to 1742 HU. While the display setting for soft tissue visualization, employs a window width (WW) of 440 HU and a window level (WL) of 55 HU, enhancing contrast for tissues such as the liver and surrounding organs. The second configuration, tailored for lung and air-filled regions, uses a broader WW of 1500 HU and a WL of -600 HU.

For the noise generation, the low-dose images were generated by inserting Poisson noise into the projection data [49], replicating quantum noise effects associated with reduced radiation exposure [50]. This simulation accounts for critical factors such as tube current modulation, bow-tie filtering, and electronic noise to accurately reflect real-world LDCT conditions [51]. The noisy projection data was then reconstructed using Filtered Back Projection (FBP). The number of detected photons at each point in the projection data follows a Poisson distribution, represented by eq. 1 [52].

$$P(k; \lambda) = \frac{\lambda^k e^{-\lambda}}{k!}, \quad k = 0, 1, 2, \dots \quad (1)$$

where  $k$  is the number of detected photons,  $\lambda$  is the mean photon count, and  $P(k; \lambda)$  is the probability of detecting  $k$  photons. This relationship highlights that noise increases as photon counts decrease, which is why LDCT scans suffer from higher noise levels [53]. FBP, while efficient, is sensitive to noise and can introduce artifacts, particularly when input projection data has low signal-to-noise ratios (SNR). Artifacts such as streaking and edge distortions are inherent to FBP but are significantly amplified when applied to noisy projection data [54]. However, due to the higher photon count and SNR, full-dose images experience minimal noise and artifacts, whereas low-dose images exhibit more pronounced artifacts and noise due to the degraded quality of projection data.

The problem formulation in this study involves addressing both quantum noise and FBP-induced artifacts to enhance LDCT image quality. A subset of the dataset is employed with a focus on abdominal imaging. The training set comprised 3,839 fully reconstructed axial plane images obtained from 20 different patients. For model evaluation, a separate test set of 421 axial slices from abdominal CT scans is used.

#### B. MODEL ARCHITECTURE

The proposed solution uses a CycleGAN model, a variant of GAN. GANs are generative networks consisting of a gener-

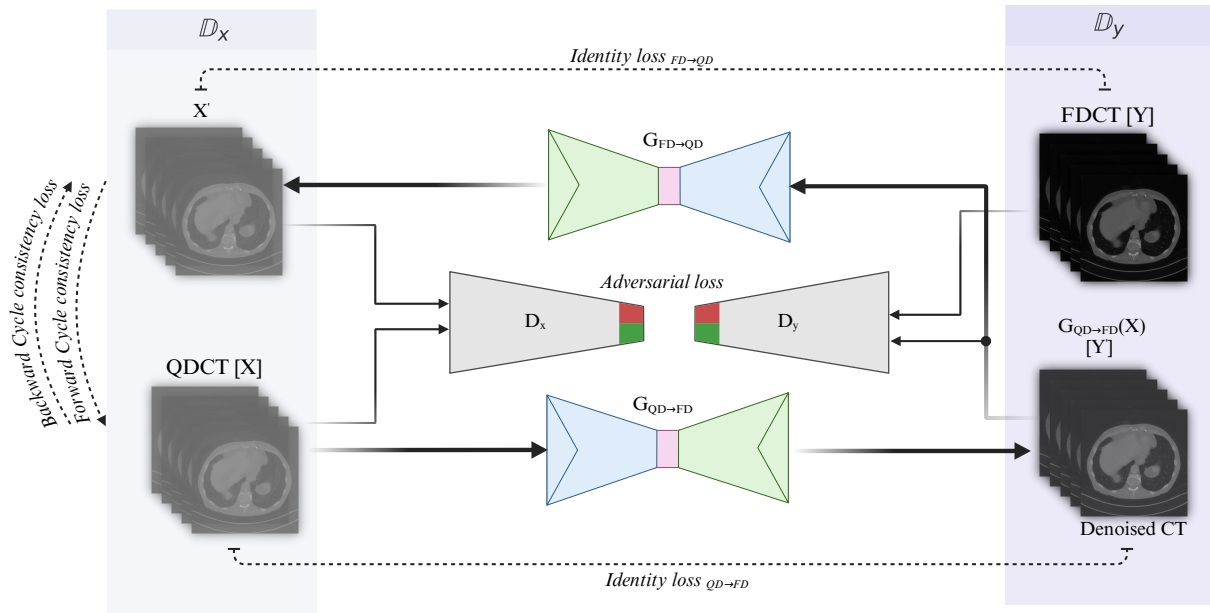


**FIGURE 3.** CycleGAN architecture for low-dose CT image denoising. The model consists of two generators ( $G_{FD \rightarrow QD}$  and  $G_{QD \rightarrow FD}$ ) and two discriminators ( $D_X$  and  $D_Y$ ). The generators aim to translate images from low-dose CT (QDCT [X]) to full-dose CT (FDCT [Y]) and vice versa. Discriminators evaluate the realism of the generated images. The *forward cycle* (QDCT  $\rightarrow$  FDCT) and *backward cycle* (FDCT  $\rightarrow$  QDCT) consistency losses ensure that the transformations between the domains preserve image content. *Adversarial loss* encourages the generators to produce images that are indistinguishable from real FDCT and QDCT images. *Identity loss* is applied to retain the characteristics of the original images when transformed into the same domain.

ator and a discriminator. The former's objective is producing realistic data, while the latter's objective is to distinguish between real and generated data [55]. Both networks are trained simultaneously, ensuring that the generator maximizes the probability of the discriminator making a mistake while the discriminator minimizes its classification error as presented in the objective function (Eq.2) [56]. Unlike GAN, CycleGAN employs multiple generators and discriminators to learn mappings between two domains, enabling image-to-image translation without requiring paired data [57].

$$\min_G \max_D V(D, G) = \mathbb{E}_{\mathbf{x} \sim p_{\text{data}}(\mathbf{x})} [\log D(\mathbf{x})] + \mathbb{E}_{\mathbf{z} \sim p_{\mathbf{z}}(\mathbf{z})} [\log(1 - D(G(\mathbf{z})))] \quad (2)$$

where  $p_{\text{data}}(\mathbf{x})$  is the distribution of the real data,  $p_{\mathbf{z}}(\mathbf{z})$  is the distribution of the noise input to the generator (often a simple distribution is used, e.g., uniform or Gaussian),  $G(\mathbf{z})$  is the generator's output, a function that maps the noise  $\mathbf{z}$  to the data space and  $D(\mathbf{x})$  is the discriminator's output, giving the probability that  $\mathbf{x}$  is real.

Although it has been primarily used as an unsupervised method, it has also significantly improved in supervised learning. In our context, the primary goal is to translate an LDCT image (domain X) to an FDCT image (domain Y). As shown in Fig. 3, dual generators enable the model to translate noisy images to clean images by the first generator, denoted as  $G_{FD \rightarrow QD}$ , while the second generator  $G_{QD \rightarrow FD}$  translates clean images back to noisy images, ensuring cycle consistency. Similarly, the first discriminator,  $D_X$ , distinguishes

between real FDCT images and generated images, while the second discriminator,  $D_Y$ , distinguishes between real LDCT images and generated LDCT images by the other cycle. This iterative process enforces cycle consistency, ensuring that an image converted from noisy to clean and back to noisy remains similar to the original [58].

### 1) The Generator

The generator,  $G$ , takes a random noise vector,  $z$ , as input and outputs a data point,  $G(z)$ , that should ideally resemble the real data [59]. The proposed generator architecture is a CNN-based UNet. UNet has been widely used in denoising images due to its encoding-decoding capabilities [60]. As shown in Fig. 4(a), it consists of three blocks of encoder and decoder with 512 convolutions bottleneck. Each block in the encoder downsamples the image by 64, 128, 256 convolutions, and the same with convolutions transpose for the decoder. Another improvement layer is added by merging the attention mechanism and residual connections to the U-Net. Specifically, a cross-attention module is embedded in each block within the model. The attention mechanism allows a model to focus on important parts within the input. It involves calculating query ( $Q$ ), key ( $K$ ) and value ( $V$ ) of input images.

In each attention block in the model, components  $Q$ ,  $K$ , and  $V$  tensors are calculated by different 2D convolution layers followed by batch normalization layer. After obtaining the three tensors, element-wise multiplication is calculated as

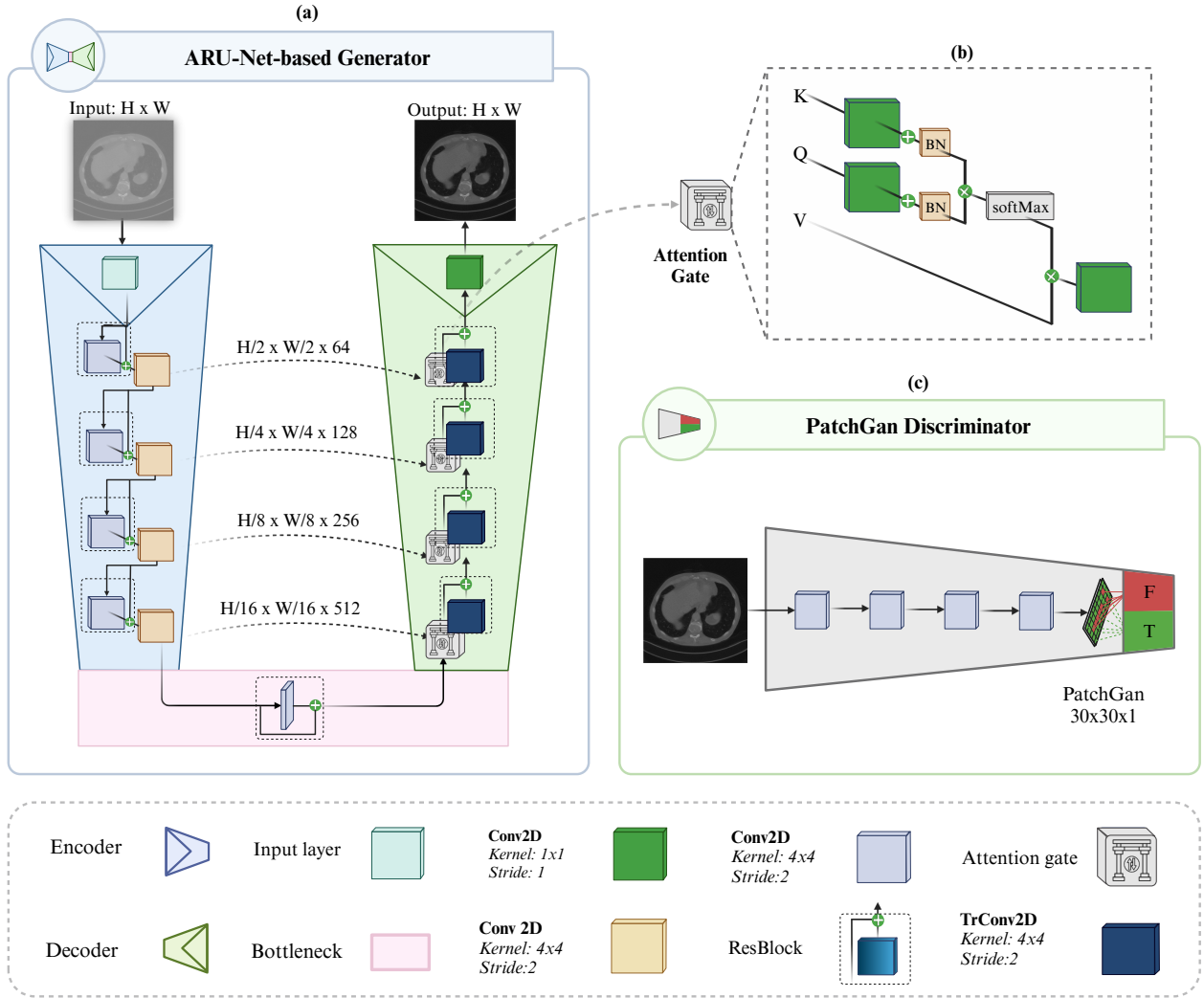


**FIGURE 4. Generators and discriminators architecture of the proposed Attention Residual U-Net CycleGAN (ARUC-GAN) for low-dose CT denoising. (a): The generator network adopts a U-Net structure with 4 downsampling and 4 upsampling layers, incorporating residual connections and the attention mechanism. (b): The attention mechanism computes the query (Q), key (K), and value (V) representations of the input features. The attention scores are calculated using the dot-product between Q and K, normalized by the softmax operation. The attended features are then combined with the original input via residual connections. (c): The PatchGAN discriminator evaluates image patches (30x30) to distinguish denoised images.**

presented in Eqn. 3 [61].

$$\text{Attention}(Q, K, V) = \text{softmax} \left( \frac{QK^T}{\sqrt{d_k}} \right) V \quad (3)$$

where  $d_k$  is the dimension of the key vectors. These features are then passed through a convolution layer with batch normalization, and dropout is added to a residual structure to obtain the final feature of this block. A residual structure uses skip connections, which allow the model to bypass one or more layers instead of using the usual forward path. This enables it to be added directly to the output of a subsequent layer, allowing the model to learn more useful features with less complexity [62]. Both forward and backward cycle generators have the same architecture that utilizes mean squared error (MSE) as a loss function. Moreover, it employs LeakyReLU as an activation function, allowing for a non-zero gradient

when the input is negative to avoid the dying ReLU problem [63]. The CycleGAN framework uses the Attention U-Net for its generators. It incorporates attention mechanisms to enhance feature refinement within the generator networks. To evaluate the contribution of CycleGAN to the overall denoising performance, an ablation study is conducted by comparing the standalone ARU-Net with the complete ARUC-GAN model.

## 2) The Discriminator

The discriminator network in the proposed architecture, shown in Fig. 4(b), is designed to distinguish between real and generated LDCT images. As an adversary, it evaluates input image patches of size  $30 \times 30$  to identify denoised images using the PatchGAN architecture. It sends feedback to the generator to improve its output and maximize its

**TABLE 1. The tuned hyperparameters of the ARUC-GAN proposed model.**

Parameter	Value
Input Size	512 × 512
Loss Function	Hybrid Function (Generator, cycle, and identity losses)
Optimizer	Adam
Initial Learning Rate	2 × 10 <sup>-3</sup>
Batch Size	8
Epochs	100

discrimination capabilities. The architecture employed is a CNN network of four layers with 64, 128, 256, and 512 convolutions. It uses LeakyRelu and batch normalization with a classification output layer returning either fake or real. The loss function employed in both discriminators is MSE.

### C. THE HYPER-PARAMETERS

The parameter that affects the most in any network is the choice of the loss function. Due to the dependency of multiple aspects in CycleGAN, a hybrid loss function is often employed, combining multiple components [64]. The first component is the generator loss, which encourages the generators,  $G_{FD \rightarrow QD}$  and  $G_{QD \rightarrow FD}$ , to produce images that are indistinguishable from real clean images  $Y$  and  $X$ , respectively. Equation 8 shows the adversarial loss of the sum of both generators.

$$\mathcal{L}_{adv} = MSE_G(G_{FD \rightarrow QD}, D_Y, X, Y) + MSE_G(G_{QD \rightarrow FD}, D_X, Y, X) \quad (8)$$

where  $X$  represents an image from the  $FD$  domain (e.g., the original domain before translation), and  $Y$  represents an image from the  $QD$  domain (e.g., the target domain after translation).  $G_{FD \rightarrow QD}$  is the generator that translates images from domain  $FD$  (source) to domain  $QD$  (target), and  $G_{QD \rightarrow FD}$  is the generator that translates images from domain  $QD$  back to domain  $FD$ .  $MSE_G$  represents the generator loss function.

Another important component is the cycle-consistency loss that ensures the image remains unchanged when translated from domain,  $X$ , to domain,  $Y$ , and then back to domain  $X$ , presented in Eq. 9.

$$\mathcal{L}_{cycle} = MAE(G_{FD \rightarrow QD}(X), G_{QD \rightarrow FD}(Y)) \quad (9)$$

where  $MAE_{cycle}$  represents the cycle loss function.

Identity loss is an important component as well. It measures the difference between the input and output images generated by the network as presented in Eq. 10. This ensures the generator produces an output that is close to the input.

$$\mathcal{L}_{id} = \lambda_{identity} (\lambda_X \cdot MAE(G_{QD \rightarrow FD}(X), X) + \lambda_Y \cdot MAE(G_{FD \rightarrow QD}(Y), Y)) \quad (10)$$

where  $\lambda_X$  and  $\lambda_Y$  are weighting factors for the identity loss in their respective domains, while  $\lambda_{identity}$  is a global weighting factor for the identity loss across both domains.

where  $\lambda_A$  and  $\lambda_B$  are hyper-parameters controlling the weight of the identity loss for each generator with a value equal to 10.  $\lambda_{identity}$  is a hyper-parameter scaling the overall importance of identity loss with value equals 0.5.

As presented in Table 1, Adam optimizer is employed with an initial learning rate of  $2e^{-3}$  linearly decaying, batch size of 8, and total epochs of 100.

The hardware configuration includes NVIDIA RTX 3060 GPU, an Intel i7-11800H CPU, and 16 GB of RAM. The models are implemented in Python 3.11 using PyTorch, which served as the primary deep learning framework with additional supporting libraries.

### D. MODEL EVALUATION

The proposed U-Net and Cycle GAN models have been evaluated and compared with multiple architectures from the literature. Quantitative evaluation metrics used for this include PSNR, RMSE, SSIM, EKI [34], as listed in Table 2.

Each metric quantifies the difference between real FDCT and the generated denoised image differently. Moreover, other aspects are considered, including visual evaluation and complexity. We also compare all models' parameter numbers and training and inference times.

## IV. RESULTS & DISCUSSION

### A. LEARNING DYNAMICS

Over 100 epochs, the training performance of the ARUC-GAN model is shown in Figure 5. Adversarial, cycle consistency, and identity losses illustrate this interaction. The cycle consistency loss is shown in Fig. 5(a) to ensure that the CT scans retain their original structure when an image is translated from one domain to the other and then back. Both generators,  $G_{FD \rightarrow QD}$  and  $G_{QD \rightarrow FD}$ , exhibit a significant drop in cycle consistency loss during the initial epochs. They completely stabilized after approximately 25 epochs. This indicates that the model effectively learns the mappings between the two domains while maintaining the structural integrity of the images. The identity loss for both  $G_{FD \rightarrow QD}$  and  $G_{QD \rightarrow FD}$  is provided in Fig. 5(b). It showed a rapid decrease in the early stages of training and remains low after approximately 25 epochs. Such behavior indicates that both generators are preserving the key characteristics of images. In Fig. 5(c,d), the adversarial losses of both generators and discriminators are presented. Both generators exhibit fluctuations in their adversarial losses throughout training, which is a characteristic behavior in adversarial models. Over the training process, both generators demonstrate steady improvement, reflected by their ability to generate more realistic images as training progresses. On the same basis, both discriminators exhibit typical fluctuations as they strive to distinguish between denoised and real images. Both discriminators learn to better assess the realism of the generated images.

**TABLE 2. Evaluation metrics employed for evaluating denoising models.**

Metric	Definition	Equation	Parameters
PSNR	Measures the peak error between the original and denoised images.	$10 \cdot \log_{10} \left( \frac{L^2}{\text{MSE}} \right)$	(4) $L$ is the maximum possible pixel value of the image.
SSIM	Indicates the similarity between two images by considering changes in structural information, luminance, and contrast.	$\frac{(2\mu_I\mu_K + C_1)(2\sigma_{IK} + C_2)}{(\mu_I^2 + \mu_K^2 + C_1)(\sigma_I^2 + \sigma_K^2 + C_2)}$	(5) $\mu_I$ and $\mu_K$ are the average values of images $I$ and $K$ respectively. $\sigma_I^2$ and $\sigma_K^2$ are the variances of $I$ and $K$ respectively. $\sigma_{IK}$ is the covariance of $I$ and $K$ . $C_1$ and $C_2$ are constants.
RMSE	A measure of the differences between predicted values by a model and the actual values.	$\sqrt{\frac{1}{MN} \sum_{i=0}^{M-1} \sum_{j=0}^{N-1} (I(i,j) - K(i,j))^2}$	(6) $I$ is the original image, $K$ is the denoised image, and $M$ and $N$ are the dimensions of the images.
EKI	Measures the preservation of edge features between the ground truth and predicted images.	$1 - \frac{\sum (E_{gr}(i,j) - E_{pred}(i,j))^2}{\sum E_{gr}(i,j)^2 + \epsilon}$	(7) $E_{gr}$ and $E_{pred}$ are the edge intensity values from the Sobel filter applied to the ground truth and predicted images, respectively. $\epsilon$ is a small constant to avoid division by zero.

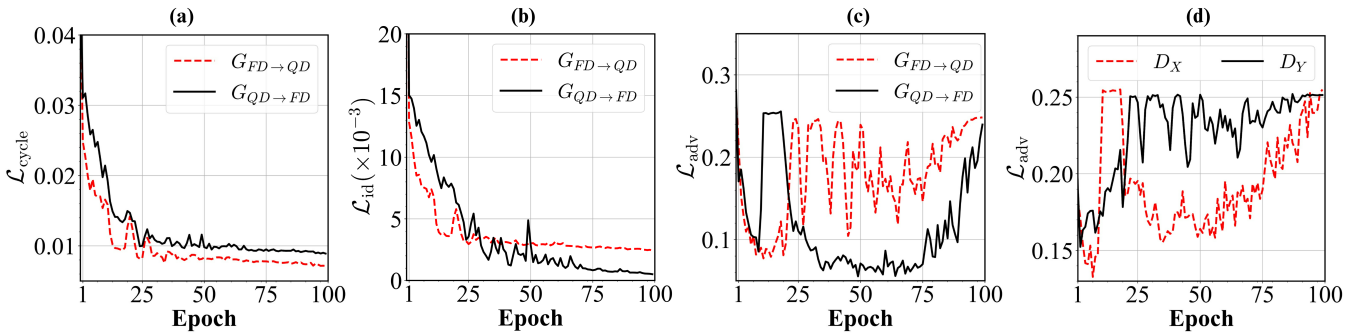


**FIGURE 5. Learning dynamics of the ARUC-GAN model over the training process. (a) Cycle consistency loss. (b) Identity loss. (c) Adversarial loss of the generators. (d) Adversarial loss of the discriminators.**

### B. DENOISING PERFORMANCE ANALYSIS

Multiple architectures from the literature are employed for evaluation and comparison along with our proposed ARU-Net and ARUC-GAN models. In the training process, Fig. 6 presents the loss curves of all models after converting the values to PSNR for unified values. It displays the performance of the training process, each experiencing a different behavior. ARU-Net and RED-CNN have nearly the same performance with the same starting point and the same rate of increase due to their shared encoder-decoder structure. In contrast, EDCNN has the same pattern with lower values. CTformer begins with low PSNR to be increased at a higher rate and stabilizes after almost 40 epochs. CycleGAN, on the other hand, shows significant fluctuations starting from a low PSNR. Nevertheless, it achieves the highest PSNR after nearly 30 epochs. These fluctuations are characteristic of GANs as the generator and discriminator engage in a competitive process. This adversarial training contributes to the observed instability and eventual improvement in PSNR. Although high PSNR indicates high-quality denoising, it can smooth out fine details and sharpness while reducing noise. Accordingly, SSIM was used as another evaluation metric,

which provides a more nuanced view of image quality, including sharpness, structural patterns, and texture.

The results presented in Table 3 highlight the superiority of the proposed ARUC-GAN model. With an SSIM of  $0.849 \pm 0.064$ , it achieves the closest match to full-dose CT images, outperforming other models in perceptual quality. Even its generator as a standalone model, ARU-Net, performs well with an SSIM of  $0.837 \pm 0.056$ , showing that the base architecture is effective before adversarial refinement. In comparison, RED-CNN, EDCNN, and CTformer exhibit lower SSIM values, with EDCNN ( $0.758 \pm 0.103$ ) and CTformer ( $0.749 \pm 0.175$ ) showing a wider spread, suggesting their performance varies across different test samples. The RMSE values further reinforce the advantage of ARUC-GAN, achieving the lowest error of  $0.018 \pm 0.007$ . This indicates that it not only reconstructs images with minimal distortions but also does so consistently. ARU-Net follows with an RMSE of  $0.023 \pm 0.009$ , while RED-CNN, EDCNN, and CTformer show higher errors. The wider standard deviation in some of these models suggests they may struggle to maintain stable reconstruction quality across different cases. PSNR results provide further insight into these differences. ARUC-GAN

**TABLE 3. Quantitative evaluation metrics on the proposed model compared to models in the literature.**

Model	LDCT	RED-CNN [65]	EDCNN [19]	CTformer [66]	This Work	
					ARU-Net	ARUC-GAN
PSNR (dB)	26.956 ± 3.794	33.488 ± 2.164	32.022 ± 2.081	32.23 ± 1.718	32.450 ± 2.492	<b>34.819 ± 2.187</b>
SSIM	0.698 ± 0.080	0.832 ± 0.095	0.758 ± 0.103	0.749 ± 0.175	0.837 ± 0.056	<b>0.849 ± 0.064</b>
RMSE	0.048 ± 0.016	0.022 ± 0.006	0.026 ± 0.007	0.025 ± 0.005	0.023 ± 0.009	<b>0.018 ± 0.007</b>
Difference PSNR (dB)	-	6.532 ± 4.370	5.066 ± 4.327	5.277 ± 4.165	5.494 ± 4.538	<b>7.863 ± 4.377</b>

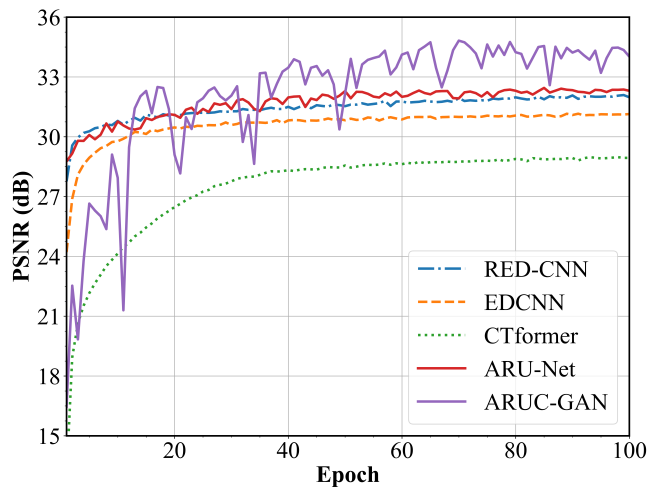


**FIGURE 6. Peak Signal-to-Noise Ratio (PSNR) curves over the training epochs for different denoising models.**

achieves the highest PSNR of  $34.819 \pm 2.187$  dB, indicating superior noise reduction while preserving critical details. Its generator alone reaches  $32.450 \pm 2.492$  dB, outperforming many traditional approaches. RED-CNN, EDCNN, and CTformer achieve lower PSNR values, with differences of  $6.532 \pm 4.370$ ,  $5.066 \pm 4.327$ , and  $5.277 \pm 4.165$  dB, respectively. Notably, CTformer exhibits the lowest standard deviation in PSNR ( $\pm 1.718$ ), meaning its performance is more stable across test samples, even if its overall accuracy is lower. This stability suggests that transformer-based architectures may be less sensitive to variations in input data, though they do not achieve the highest fidelity.

The proposed CycleGAN outperforms other models in all aspects, indicating the generation of the sharpest and most structurally accurate images with minimal noise and blurring compared to literature models. Furthermore, the CycleGAN generator with attention to the U-Net structure has the highest SSIM compared to literature models. Nevertheless, RED-CNN performed better in terms of PSNR. This demonstrates that RED-CNN has less noisy prediction with more loss of fine details than our U-Net. At the same time, EDCNN shows the highest error among the tested models, indicating more significant smoothing and loss of details. Finally, all literature models improve LDCT images, but they are still lagging behind the proposed model. Additionally, EKI was calculated to assess the preservation of edge structures in denoised images.

The results show that ARUC-GAN achieves a mean EKI value of 0.835, indicating superior edge preservation, while the ARU-Net achieves a mean EKI of 0.823.

### C. VISUAL ANALYSIS OF DENOISING RESULTS

The quantitative results show that ARUC-GAN is good at denoising low-dose CT images, but a qualitative visual assessment is still needed to see how well fine details, texture, and structural integrity are kept. Visual evaluation presented in Fig. 7 is conducted, showing the difference in multiple patches in a denoised sample from each model. The original test input and target are NDCT and LDCT, while the other snippets are predictions from the presented models. RED-CNN shows consistently strong performance in structural preservation, often achieving the second-highest SSIM scores across most cases, indicating that it effectively maintains key structural patterns and edges. However, despite its strong SSIM performance, RED-CNN tends to have lower PSNR values, as seen in the third case. This occurs because RED-CNN, while preserving structure, applies aggressive noise reduction that causes smoothing of fine details and texture, which impacts pixel-level fidelity measured by PSNR. This trade-off between high SSIM and relatively low PSNR reflects its focus on global structural consistency at the expense of localized pixel accuracy. CTformer shows better contrast and edge clarity, benefiting from transformer-based attention mechanisms that can better capture long-range dependencies. Despite this, it struggles with subtle details, particularly under complex noise patterns, where local features are lost due to less precise feature extraction. As a result, it achieves moderate SSIM and PSNR performance, sometimes close to but not exceeding the top models. EDCNN performs reasonably well in balancing noise suppression and edge preservation. It is slightly better at maintaining sharp edges compared to most other models. However, EDCNN's attempts to enhance edges still lead to smoothing artifacts in other regions, resulting in moderate SSIM and PSNR scores. ARU-Net is generally comparable to the other models and performs well in noise reduction and detail preservation. However, it does not consistently outperform them and sometimes underperforms, as in case 2, where RED-CNN and CTformer surpass it. One of ARU-Net's limitations is its tendency to oversmooth finer textures, leading to a slight loss of detail in some regions. While ARU-Net excels in scenarios where balancing structure and texture is less complex, it struggles to handle

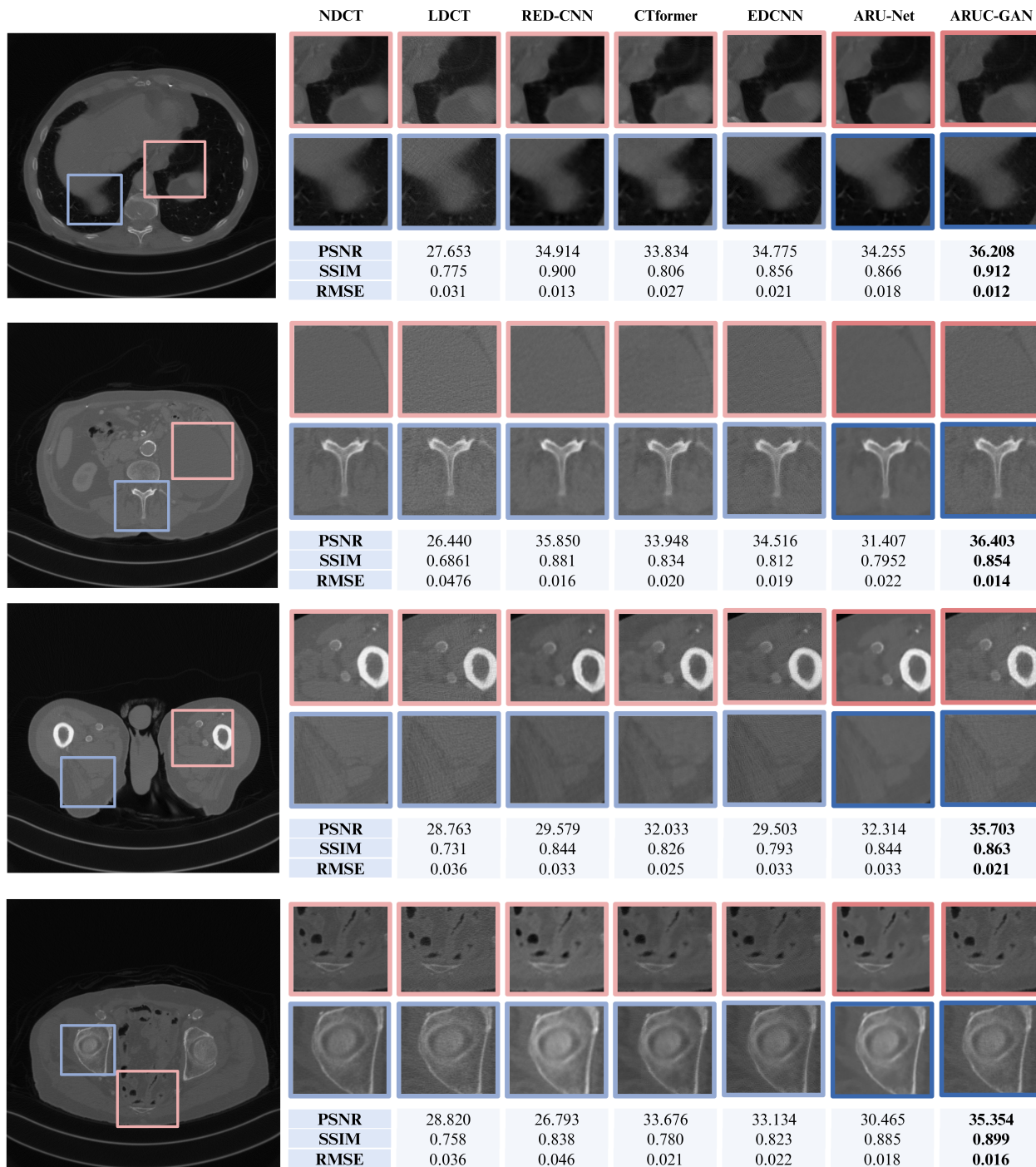


**FIGURE 7.** Visual comparison of denoised CT scans using ARUC-GAN and state-of-the-art models.

more intricate noise patterns. Finally, ARUC-GAN shows the most consistent performance among all models. It achieves the highest PSNR and SSIM in most cases, successfully balancing global structural preservation and localized detail accuracy. This superior performance stems from its ability to handle complex, non-uniform noise without over-smoothing, making it particularly suitable for denoising tasks that require

both texture fidelity and structural integrity.

#### D. DEPLOYMENT AND COMPUTATIONAL FEASIBILITY

Initial assessments with commodity hardware configuration using an Intel i7-11800H CPU @2.30GHz show that general-purpose consumer devices are sufficient for the inference of the ARUC-GAN model. The inference time was quantified

**TABLE 4. Comparison of computational demands in terms of model parameters, training time, and inference time (model latency).**

Models	No. of Parameters	Training Time (s)	Inference Time
RED-CNN [65]	$1.8 \times 10^6$	10,200	$2.00 \pm 1.10 \mu\text{s}$
EDCNN [19]	$8.1 \times 10^4$	4,800	$3.50 \pm 0.632 \mu\text{s}$
CTformer [66]	$1.7 \times 10^6$	7,400	$12.8 \pm 0.492 \text{ s}$
ARU-Net	$1.6 \times 10^7$	<b>3,371</b>	$2.60 \pm 0.802 \mu\text{s}$
ARUC-GAN	G: $2 \times 1.6 \times 10^7$ D: $2 \times 6.6 \times 10^5$	21,000	$3.00 \pm 0.632 \mu\text{s}$

by measuring the duration of a single forward pass through the model under standardized conditions. To ensure statistical reliability, multiple inference runs were conducted, and the mean and standard deviation of the inference time per sample were reported. Table 4 presents a comparative analysis of model architecture complexity, measured by the number of parameters, training time, and inference speed. With 32 M parameters in the generators and 1.32 M parameters in the discriminators, the ARUC-GAN manages to reach an average inference time of  $3.00 \mu\text{s}$ . ARU-Net is a more lightweight solution that maintains acceptable accuracy. In addition, ARUC-GAN outperforms CTformer, which has a much longer inference time of 12.8 s, and is on par with models like RED-CNN ( $2.00 \mu\text{s}$ ) and EDCNN ( $3.50 \mu\text{s}$ ). For the CTformer, this difference is likely caused by the computationally intensive self-attention algorithms and high-dimensional matrix multiplications that are part of the transformer-based design.

While real-time processing is not essential for CT imaging, certain applications, such as 4D CT in interventional procedures, need near-real-time imaging to monitor respiratory motion or aid biopsies [67], [68]. Hence, rapid and effective inference is essential for optimizing clinical operations. Accelerated denoising minimizes image reconstruction durations for more responsive diagnostic decisions. Hence, AI-driven denoising models have to balance accuracy and computational efficiency for clinical applicability. In this regard, ARUC-GAN is a viable candidate for smart health application deployment since it features powerful denoising capabilities without adding excessive computational overhead. In situations demanding high throughput or low latency requirements, further optimizations such as model quantization, pruning, and knowledge distillation can be explored to enhance inference efficiency without compromising model fidelity, including reconstruction accuracy and denoising [69]. Moreover, hardware accelerators like FPGAs and ASICs may enhance model execution for resource-constrained medical imaging equipment [70]–[72]. However, for the majority of applications, ARUC-GAN attains a balance between inference speed and denoising efficiency on consumer-grade general-purpose. This allows straightforward incorporation into existing healthcare workflows.

## V. CONCLUSIONS AND FUTURE DIRECTIONS

This study presented the ARUC-GAN architecture to enhance LDCT imaging without requiring projection data. The integration of attention mechanisms and residual learning

within the CycleGAN framework has demonstrated superior performance in tackling the complex noise patterns inherent in LDCT imaging. Quantitative and qualitative evaluations demonstrated the proposed model's robustness, with notable improvements in structural integrity and image fidelity. These enhancements contribute to making LDCT a more viable alternative for routine clinical diagnostics with reduced radiation exposure for safer and more time-efficient imaging. Furthermore, the computational efficiency of ARUC-GAN facilitates its straightforward integration into medical imaging processes without requiring excessive resource demands. Given its effectiveness in noise suppression and feature preservation, this architecture can be extended to other denoising tasks in medical imaging and beyond. Future work will focus on enlarging the dataset with greater variability, including different noise levels and imaging modalities, to further improve the model's generalizability and performance.

## REFERENCES

- [1] H. Wang, J. Huang, G. Wang, H. Lu, and W. Wang, "Contactless patient care using hospital iot: Cctv-camera-based physiological monitoring in ICU," *IEEE Internet Things J.*, vol. 11, no. 4, pp. 5781–5797, 2024.
- [2] P. Spachos, S. Gregori, and M. J. Deen, "Voice activated iot devices for healthcare: Design challenges and emerging applications," *IEEE Trans. Circuits Syst. II Express Briefs*, vol. 69, no. 7, pp. 3101–3107, 2022.
- [3] Z. Jiang, V. van Zoest, W. Deng, E. C. H. Ngai, and J. Liu, "Leveraging machine learning for disease diagnoses based on wearable devices: A survey," *IEEE Internet Things J.*, vol. 10, no. 24, pp. 21959–21981, 2023.
- [4] D. Djenouri, R. Laidi, Y. Djenouri, and I. Balasingham, "Machine learning for smart building applications: Review and taxonomy," *ACM Comput. Surv.*, vol. 52, no. 2, pp. 24:1–24:36, 2019.
- [5] M. Mansour, M. Saeed Darweesh, and A. Soltan, "Wearable devices for glucose monitoring: A review of state-of-the-art technologies and emerging trends," *Alexandria Engineering Journal*, vol. 89, pp. 224–243, 2024.
- [6] R. T. Sadia, J. Chen, and J. Zhang, "Ct image denoising methods for image quality improvement and radiation dose reduction," *Journal of Applied Clinical Medical Physics*, vol. 25, 2 2024.
- [7] United Nations Scientific Committee on the Effects of Atomic Radiation (UNSCEAR), *Sources, Effects and Risks of Ionizing Radiation: UNSCEAR 2020/2021 Report, Annex A: Evaluation of Medical Exposure to Ionizing Radiation*. New York: United Nations, 2022.
- [8] J. M. Meulepas, C. M. Ronckers, A. M. Smets, R. A. Nijelstein, P. Gradowska, C. Lee, A. Jahnen, M. Van Straten, M.-C. Y. De Wit, B. Zonnenberg, W. M. Klein, J. H. Merks, O. Visser, F. E. Van Leeuwen, and M. Hauptmann, "Radiation exposure from pediatric ct scans and subsequent cancer risk in the netherlands," *Journal of the National Cancer Institute*, vol. 111, no. 3, p. 256 – 263, 2019.
- [9] C. Pozzessere, C. von Garnier, and C. Beigelman-Aubry, "Radiation exposure to low-dose computed tomography for lung cancer screening: should we be concerned?," *Tomography*, vol. 9, no. 1, pp. 166–177, 2023.
- [10] M. Han and J. Baek, "Direct estimation of the noise power spectrum from patient data to generate synthesized ct noise for denoising network training," *Medical physics*, vol. 51, no. 3, pp. 1637–1652, 2024.
- [11] P. Sengodan, K. Srinivasan, R. Pichamuthu, and S. Matheswaran, "Early detection and classification of malignant lung nodules from ct images: An optimal ensemble learning," *Expert Systems with Applications*, vol. 229, p. 120361, 2023.
- [12] D. Hussain and Y. Hyeon Gu, "Exploring the impact of noise and image quality on deep learning performance in dxa images," *Diagnostics*, vol. 14, no. 13, p. 1328, 2024.
- [13] S. Puneeth, B. Poornima, B. PremaSudha, N. Patil, B. Puneetha, and R. B. Jadekar, "An effective noise removal technique for enhancing ischemic brain stroke computed tomography images," in *2024 First International Conference on Innovations in Communications, Electrical and Computer Engineering (ICICEC)*, pp. 1–6, IEEE, 2024.
- [14] F. Zhang, H. Yao, E. Langzam, Q. Meng, X. Meng, R. J. van der Geest, C. Luo, T. Zhang, J. Li, J. Xiong, et al., "Detectability of intracranial vessel

- wall atherosclerosis using black-blood spectral ct: a phantom and clinical study," *European Radiology Experimental*, vol. 8, no. 1, p. 78, 2024.
- [15] J. Zhang, Y. Niu, Z. Shangguan, W. Gong, and Y. Cheng, "A novel denoising method for ct images based on u-net and multi-attention," *Computers in Biology and Medicine*, vol. 152, p. 106387, 2023.
- [16] P. Schindler and M. Gerwing, "Using deep learning-based denoising and iterative reconstruction to reduce radiation exposure – how low can we go?," *European Journal of Radiology*, vol. 173, p. 111376, 2024.
- [17] H. Chen, Y. Zhang, W. Zhang, P. Liao, K. Li, J. Zhou, and G. Wang, "Low-dose ct via convolutional neural network," *Biomedical Optics Express*, vol. 8, no. 2, p. 679 – 694, 2017.
- [18] E. Kang, J. Min, and J. C. Ye, "A deep convolutional neural network using directional wavelets for low-dose x-ray ct reconstruction," *Medical Physics*, vol. 44, no. 10, p. e360–e375, 2017.
- [19] T. Liang, Y. Jin, Y. Li, and et al., "Edcnn: Edge enhancement-based densely connected network with compound loss for low-dose ct denoising," in *2020 15th IEEE International Conference on Signal Processing (ICSP)*, vol. 1, pp. 193–198, IEEE, 2020.
- [20] S. Gou, W. Liu, C. Jiao, and et al., "Gradient regularized convolutional neural networks for low-dose ct image enhancement," *Physics in Medicine & Biology*, vol. 64, no. 16, p. 165017, 2019.
- [21] M. Gholizadeh-Ansari, J. Alirezaie, and P. Babyn, "Deep learning for low-dose ct denoising using perceptual loss and edge detection layer," *Journal of Digital Imaging*, vol. 33, no. 2, pp. 504–515, 2020.
- [22] J. Ming, B. Yi, Y. Zhang, and et al., "Low-dose ct image denoising using classification densely connected residual network," *KSI Transactions on Internet and Information Systems (TIIS)*, vol. 14, no. 6, pp. 2480–2496, 2020.
- [23] L. Yang, H. Shangguan, X. Zhang, and et al., "High-frequency sensitive generative adversarial network for low-dose ct image denoising," *IEEE Access*, vol. 8, pp. 930–943, 2019.
- [24] D. Wu, K. Kim, G. E. Fakhri, and et al., "A cascaded convolutional neural network for x-ray low-dose ct image denoising," *arXiv preprint arXiv:1705.04267*, 2017.
- [25] S. Ataei, J. Alirezaie, and P. Babyn, "Cascaded convolutional neural networks with perceptual loss for low dose ct denoising," in *2020 International Joint Conference on Neural Networks (IJCNN)*, pp. 1–5, IEEE, 2020.
- [26] P. Singh, M. Diwakar, R. Gupta, and et al., "A method noise-based convolutional neural network technique for ct image denoising," *Electronics*, vol. 11, no. 21, p. 3535, 2022.
- [27] F. Yu and V. Koltun, "Multi-scale context aggregation by dilated convolutions," 2016.
- [28] M. Gholizadeh-Ansari, J. Alirezaie, and P. Babyn, "Low-dose ct denoising with dilated residual network," in *2018 40th Annual International Conference of the IEEE Engineering in Medicine and Biology Society (EMBC)*, pp. 5117–5120, IEEE, 2018.
- [29] X. Jiang, Y. Jin, and Y. Yao, "Low-dose ct lung images denoising based on multiscale parallel convolution neural network," *Visual Computer*, vol. 37, no. 8, pp. 2419–2431, 2021.
- [30] I. Shiri, A. Akhavanallaf, A. Sanaat, and et al., "Ultra-low-dose chest ct imaging of covid-19 patients using a deep residual neural network," *European Radiology*, vol. 31, no. 3, pp. 1420–1431, 2021.
- [31] W. Yang, H. Zhang, J. Yang, J. Wu, X. Yin, Y. Chen, H. Shu, L. Luo, G. Coatrieux, Z. Gui, and Q. Feng, "Improving low-dose ct image using residual convolutional network," *IEEE Access*, vol. 5, pp. 24698–24705, 2017.
- [32] X. Yin, Q. Zhao, J. Liu, and et al., "Domain progressive 3d residual convolution network to improve low-dose ct imaging," *IEEE Transactions on Medical Imaging*, vol. 38, no. 12, pp. 2903–2913, 2019.
- [33] S. K. Panigrahi, S. K. Tripathy, A. Bhowmick, S. K. Satapathy, P. Barsocchi, and A. K. Bhoi, "Multi-scale based approach for denoising real-world noisy image using curvelet thresholding: Scope and beyond," *IEEE Access*, vol. 12, pp. 25090–25105, 2024.
- [34] S. K. Panigrahi and S. Gupta, "Phase-preserved curvelet thresholding for image denoising," *Journal of The Institution of Engineers (India): Series B*, vol. 103, no. 5, pp. 1719–1731, 2022.
- [35] Şaban Öztürk, O. C. Duran, and T. Çukur, "Denomamba: A fused state-space model for low-dose ct denoising," 2024.
- [36] O. F. Atli, B. Kabas, F. Arslan, A. C. Demirtas, M. Yurt, O. Dalmaz, and T. Çukur, "I2i-mamba: Multi-modal medical image synthesis via selective state space modeling," 2024.
- [37] J. M. Wolterink, T. Leiner, M. A. Viergever, and et al., "Generative adversarial networks for noise reduction in low-dose ct," *IEEE Transactions on Medical Imaging*, vol. 36, no. 12, pp. 2536–2545, 2017.
- [38] X. Yi and P. Babyn, "Sharpness-aware low-dose ct denoising using conditional generative adversarial network," *Journal of Digital Imaging*, vol. 31, pp. 655–669, 2018.
- [39] C. You, Q. Yang, H. Shan, and et al., "Structurally-sensitive multi-scale deep neural network for low-dose ct denoising," *IEEE Access*, vol. 6, pp. 41839–41855, 2018.
- [40] Y. Ma, B. Wei, P. Feng, and et al., "Low-dose ct image denoising using a generative adversarial network with a hybrid loss function for noise learning," *IEEE Access*, vol. 8, pp. 67519–67529, 2020.
- [41] Q. Yang, P. Yan, Y. Zhang, and et al., "Low-dose ct image denoising using a generative adversarial network with wasserstein distance and perceptual loss," *IEEE Transactions on Medical Imaging*, vol. 37, no. 6, pp. 1348–1357, 2018.
- [42] Z. Li, W. Shi, Q. Xing, and et al., "Low-dose ct image denoising with improving wgan and hybrid loss function," *Computational and Mathematical Methods in Medicine*, vol. 26, p. 2973108, 2021.
- [43] L. Yang, H. Shangguan, X. Zhang, A. Wang, and Z. Han, "High-frequency sensitive generative adversarial network for low-dose ct image denoising," *IEEE Access*, vol. 8, pp. 930–943, 2020.
- [44] J. Liu, H. Jiang, F. Ning, and et al., "Dfsne-net: deviant feature sensitive noise estimate network for low-dose ct denoising," *Computers in Biology and Medicine*, vol. 149, p. 106061, 2022.
- [45] J. Chi, C. Wu, X. Yu, and et al., "Single low-dose ct image denoising using a generative adversarial network with modified u-net generator and multi-level discriminator," *IEEE Access*, vol. 8, pp. 133470–133487, 2020.
- [46] Z. Huang, J. Zhang, Y. Zhang, and et al., "Du-gan: generative adversarial networks with dual-domain u-net-based discriminators for low-dose ct denoising," *IEEE Transactions on Instrumentation and Measurement*, vol. 71, pp. 1–12, 2021.
- [47] E. Kang, H. J. Koo, D. H. Yang, and et al., "Cycle-consistent adversarial denoising network for multiphase coronary ct angiography," *Medical Physics*, vol. 46, no. 2, pp. 550–562, 2019.
- [48] C. Tang, J. Li, L. Wang, and et al., "Unpaired low-dose ct denoising network based on cycle-consistent generative adversarial network with prior image information," *Computational and Mathematical Methods in Medicine*, vol. 2019, 2019.
- [49] T. R. Moen, B. Chen, D. R. Holmes, X. Duan, Z. Yu, L. Yu, S. Leng, J. G. Fletcher, and C. H. McCollough, "Low-dose ct image and projection dataset," *Medical Physics*, vol. 48, no. 2, pp. 902–911, 2021.
- [50] Q. Ding, Y. Long, X. Zhang, and J. A. Fessler, "Statistical image reconstruction using mixed poisson-gaussian noise model for x-ray ct," *arXiv preprint arXiv:1801.09533*, 2018.
- [51] C. Kim and J. Kim, "Realistic simulation of reduced-dose ct with noise modeling and sinogram synthesis using dicom ct images," *Medical physics*, vol. 41, p. 011901, 01 2014.
- [52] Y. Han, X. Liu, N. Zhang, Y. Wang, M. Ju, and Y. Ding, "Ldct image denoising algorithm based on two-dimensional variational mode decomposition and dictionary learning," *Scientific Reports*, vol. 14, no. 1, p. 17487, 2024.
- [53] M. Danielsson, M. Persson, and M. Sjölin, "Photon-counting x-ray detectors for ct," *Physics in Medicine & Biology*, vol. 66, no. 3, p. 03TR01, 2021.
- [54] X. Tan, X. Liu, K. Xiang, J. Wang, and S. Tan, "Deep filtered back projection for ct reconstruction," *IEEE Access*, 2024.
- [55] P. Salehi, A. Chalechale, and M. Taghizadeh, "Generative adversarial networks (gans): An overview of theoretical model, evaluation metrics, and recent developments," 2020.
- [56] K. S. Lee, N.-T. Tran, and N.-M. Cheung, "Infomax-gan: Improved adversarial image generation via information maximization and contrastive learning," in *Proceedings of the IEEE/CVF Winter Conference on Applications of Computer Vision (WACV)*, pp. 3942–3952, January 2021.
- [57] R. K. Senapati, R. Satvika, A. Anmandla, G. Ashesh Reddy, and C. Anil Kumar, "Image-to-image translation using pix2pix gan and cycle gan," in *Data Intelligence and Cognitive Informatics (I. J. Jacob, S. Piramuthu, and P. Falkowski-Gilski, eds.)*, (Singapore), pp. 573–586, Springer Nature Singapore, 2024.
- [58] T. Kwon and J. C. Ye, "Cycle-free cyclegan using invertible generator for unsupervised low-dose ct denoising," *IEEE Transactions on Computational Imaging*, vol. 7, pp. 1354–1368, 2021.

- [59] T. Zhou, Q. Li, H. Lu, Q. Cheng, and X. Zhang, "Gan review: Models and medical image fusion applications," *Information Fusion*, vol. 91, pp. 134–148, 2023.
- [60] J. Zhang, W. Gong, L. Ye, F. Wang, Z. Shangguan, and Y. Cheng, "A review of deep learning methods for denoising of medical low-dose ct images," *Computers in Biology and Medicine*, vol. 171, p. 108112, 2024.
- [61] X. Wang, L. Sun, C. Lu, and B. Li, "A novel transformer network with a cnn-enhanced cross-attention mechanism for hyperspectral image classification," *Remote Sensing*, vol. 16, no. 7, 2024.
- [62] R. Wang, Chencho, S. An, J. Li, L. Li, H. Hao, and W. Liu, "Deep residual network framework for structural health monitoring," *Structural Health Monitoring*, vol. 20, no. 4, pp. 1443–1461, 2021.
- [63] X. Qi, Y. Wei, X. Mei, R. Chellali, and S. Yang, "Comparative analysis of the linear regions in relu and leakyrelu networks," in *Neural Information Processing* (B. Luo, L. Cheng, Z.-G. Wu, H. Li, and C. Li, eds.), (Singapore), pp. 528–539, Springer Nature Singapore, 2024.
- [64] Y. Ma, B. Wei, P. Feng, P. He, X. Guo, and G. Wang, "Low-dose ct image denoising using a generative adversarial network with a hybrid loss function for noise learning," *IEEE Access*, vol. 8, pp. 67519–67529, 2020.
- [65] H. Chen, Y. Zhang, M. Kalra, and et al., "Low-dose ct with a residual encoder-decoder convolutional neural network," *IEEE Transactions on Medical Imaging*, vol. 36, no. 12, pp. 2524–2535, 2017.
- [66] D. Wang, F. Fan, Z. Wu, R. Liu, F. Wang, and H. Yu, "Ctformer: convolution-free token2token dilated vision transformer for low-dose ct denoising," *Physics in Medicine & Biology*, vol. 68, p. 065012, Mar. 2023.
- [67] A. Graas, S. B. Coban, K. J. Batenburg, and F. Lucka, "Just-in-time deep learning for real-time x-ray computed tomography," *Scientific Reports*, vol. 13, p. 20070, 11 2023.
- [68] T. Reynolds, O. Dillon, Y. Ma, N. Hindley, J. W. Stayman, and M. Bazalova-Carter, "Investigating 4d respiratory cone-beam ct imaging for thoracic interventions on robotic c-arm systems: a deformable phantom study," *Physical and Engineering Sciences in Medicine*, vol. 47, pp. 1751–1762, 12 2024.
- [69] Y. Liang, J. Tan, Z. Xie, Z. Chen, D. Lin, and Z. Yang, "Research on convolutional neural network inference acceleration and performance optimization for edge intelligence," *Sensors*, vol. 24, no. 1, 2024.
- [70] A. Mouri Zadeh Khaki and A. Choi, "Optimizing deep learning acceleration on fpga for real-time and resource-efficient image classification," *Applied Sciences*, vol. 15, no. 1, 2025.
- [71] R. Wu, X. Guo, J. Du, and J. Li, "Accelerating neural network inference on fpga-based platforms—a survey," *Electronics*, vol. 10, no. 9, 2021.
- [72] X. Xie, W. Yang, Y. He, and Y. Chen, "A reconfigurable gc-cyclegan based on convolutional optimization," in *Proceedings of the 2023 6th International Conference on Artificial Intelligence and Pattern Recognition*, AIPR '23, (New York, NY, USA), p. 676–682, Association for Computing Machinery, 2024.



**DJAMEL DJENOURI** is with the University of the West of England (UWE), Bristol, UK, since Dec 2019, where he is leading many research projects. He obtained the Doctorate in Computer Science from the University of Science and Technology (USTHB), in 2007. He was granted a post-doctoral fellowship from the European Research Consortium on Informatics and Mathematics (ERCIM) and worked at the Norwegian University of Science and Technology (NTNU), Norway, from 2008 to 2009. He was a senior research scientist (Director of Research) and deputy director at the CERIST, Algiers. He also served as adjunct full professor at Blida university and the EMP polytechnic university, Algiers. He is currently working on topics related to the internet of things, wireless and mobile networks, network security, machine learning and applications for smart cities and green applications. He has been conducting several research projects with international collaborations as the principal investigator for many of them. He participated in many international conferences worldwide and gave many keynotes and plenary-session talks. He has been granted international mobility internships for visits to many universities including NTNU, SICS (Stockholm), university of Cape Town, UPC Barcelona, JMU Liverpool, UTC (Compiègne), Nuertingen Geislingen university (Stuttgart), university of Padova, Sousse university, university of Oxford, etc. He published more than 150 papers in international peer-reviewed journals and conference proceedings, two books, and he is holding two national patents. He was reported amongst the top 2% most cited scientists in the annual Stanford university releases (2021-2023 releases), and ranked on top 0.5% of all scholars worldwide by ScholarGPS in his research fields. He voluntarily contributed to the organization of many conferences and workshops, and he served as TPC member of many international conferences, as well as guest editor, member of editorial board for many journals including IEEE Trans on Man Sys and Cybernetics, and Future Internet journal. He is a senior member of Association of Commuting Machinery (ACM), member of the Arab/German Young Academy of Science and Humanities (AGYA), and fellow of the UK Higher Education Academy (HEA).



**MOHAMMAD MANSOUR** (Member, IEEE) received the B.Sc. degree in electronics and communication engineering from Al-Azhar University, Cairo, Egypt, in 2020, and the master's degree from Nile University (NU), Giza, Egypt, in 2024. He is currently pursuing the Ph.D. degree with McMaster University, Hamilton, ON, Canada.

He was a Research Assistant with TU Clausthal University, Clausthal-Zellerfeld, Germany. He was also a Research Assistant with the Nanoelectronics

Integrated Systems Center (NISC), NU. He is working as a Research Assistant with the Department of Electrical and Computer Engineering, McMaster University. His research interests include biomedical sensors, the Internet of Things (IoT), communication protocols, embedded systems, wireless sensor networks, hardware acceleration, and artificial intelligence.

Mr. Mansour won the Best Research Project Prize from Port Said University on the "Second Water Day 2022."



**LOBNA A. SAID** (Senior Member, IEEE) is a full-time Associate Professor at the Faculty of Engineering and Applied Science, Nile University (NU). She is the director of the Microelectronics System Design Master Program (MSD) and the former Co-director of the Nanoelectronics Integrated System Design Research Center (NISC). She received her B.Sc., M.Sc., and PhD in electronics and electrical communications from Cairo University, Egypt, in 2007, 2011, and 2016, respectively. She has over 200 publications distributed between high-impact journals, conferences, and book chapters. She has an H-index of 31, as reported by the Scopus database. Her interdisciplinary research interests include modeling, control, optimization techniques, analog and digital integrated circuits, fractional-order circuits and systems, Memristors, non-linear analysis, and chaos theory. She was involved in many national/international research grants as a PI, Co-PI, or Senior Researcher/Member. She is the Vice-Chair of the technical Chapters of the IEEE Egypt Section and the Chair of the IEEE Computational Intelligence Egypt Chapter. She is the Counselor of the IEEE NU student branch 2018-present. She has been the Co-chair of WIE in the IEEE CAS Egypt Technical Chapter since 2021. She won the state encouragement award for the year 2019 in engineering science. She received the Excellence Award from the Center for the Development of Higher Education and Research in 2019 for the best PhD thesis in 2016. She won the Dr Hazem Ezzat Prize for Outstanding Researcher NU 2019 and 2020. Her name was in the Top 2 percent of Scientists, According to the Stanford Report for 2019, 2020, and 2021. She has received the Recognized Reviewer Award from many international journals. She was awarded the IEEE Outstanding Branch Counselor & Branch Chapter Advisor Award in 2021. In 2022, she received the Junior Faculty Development Program (JFDP) from Fulbright. In 2023, She received the Africa Science Leadership Programme (ASLP) fellowship from The University of Pretoria and the Global Young Academy, with the support of the Robert Bosch Stiftung. In 2019, she was selected as a member of the Egyptian Young Academy of Sciences (EYAS) to empower and encourage young Egyptian scientists in science and technology and build knowledge-based societies. In 2020, she was elected as the Co-Chair of EYAS. Furthermore, in 2020, she was selected to be an African Academy of Science (AAS) affiliate member. In 2020, she was also chosen to be a Member of the Arab-German Young Academy of Sciences and Humanities (AGYA). In 2021, she was selected to be a Member of the Council for Future Studies and Risk Management, ASRT, Egypt. Additionally, she served on the technical and organizing committees of many international conferences, organized special sessions, and was selected as a TWAS Young Affiliate. In 2022, she was elected as a steering committee member of AGYA. In 2022, she joined the editorial board of Four journals belonging to these publishers: Elsevier, MDPI, and Frontiers. In 2023, she was elected to be the co-president of AGYA and selected to be a Member of the Organization for Women in Science for the Developing World (OWSD)



**SHAHID LATIF** (Member IEEE) received a Ph.D. in Electronic Science and Technology at the School of Information Science and Technology, Fudan University, Shanghai, China, in January 2024. He currently works as a Research Associate at the School of Computing and Creative Technologies, UWE Bristol, United Kingdom. In addition to his academic pursuits, he has also gained practical experience as a visiting researcher at Edinburgh Napier University, UK, and Prince Sultan University, Saudi Arabia. He regularly serves as an invited reviewer for numerous world-leading journals, including Elsevier Journal of Industrial Information Integration, IEEE Transactions on Industrial Informatics, IEEE Transactions on Systems, Man, and Cybernetics: Systems, Nature Scientific Reports, and IEEE Access.



**AHMED MAALEL** holds a PhD in Computer Science (2015) and Habilitation to Direct Research (HDR) (2022) from the National School of Computer Science (ENSI, Tunisia). He is an Associate Professor at the Higher Institute of Applied Science and Technology of Sousse (ISSATSo), University of Sousse, Tunisia, and a researcher at the RIADI laboratory at ENSI. His research focuses on Artificial Intelligence, Decision Support Systems, Crisis Management, Gamification of Learning, and the Semantic Web.

Dr. Maalel is an IEEE Senior Member, Co-Founder and President of the Association of Scientific Research and Innovation in Computer Science (ARSII), and has served as a technical chair, TPC member, and reviewer for various international conferences and journals. From 2017 to 2021, he was the Horizon 2020 National Contact Point for ICT and Horizon Europe NCP for digital cluster at the Tunisian Ministry of Higher Education and Scientific Research.

Dr. Maalel was a member of the University of Sousse Council (2020-2023) and leads the Project Management Office at the university, contributing to strategic initiatives and collaboration efforts.



**AMEER M. S. ABDELHADI** is an assistant professor of Computer Engineering in the Department of Electrical and Computer Engineering at McMaster University. He obtained his PhD in Computer Engineering from the University of British Columbia in 2016. Prior to joining McMaster, Dr. Abdelhadi held various academic positions as a research fellow and lecturer at the University of Toronto, Imperial College London, and Simon Fraser University. Before pursuing his graduate studies, he held multiple design and research positions in the semiconductor industry. Dr. Abdelhadi's research interests span multiple areas, including application-specific custom-tailored computer architecture and hardware acceleration, hardware-efficient deep learning, neurotechnology, reconfigurable computing, and asynchronous circuits.

...